

# Control over Aspect Ratio and Polymer Spatial Distribution of 2D Platelets via Living Crystallization-Driven Self-Assembly

Tianlai Xia,<sup>○</sup> Laihui Xiao,<sup>○</sup> Kaiwen Sun, Julia Y. Rho, Yujie Xie, Sam J. Parkinson, Leire Sangroniz, Jian Zhang, Jiaping Lin, Alejandro J. Müller, Liang Gao, Andrew P. Dove,<sup>\*</sup> and Rachel K. O'Reilly<sup>\*</sup>



Cite This: *Macromolecules* 2024, 57, 11210–11220



Read Online

ACCESS |



Metrics & More

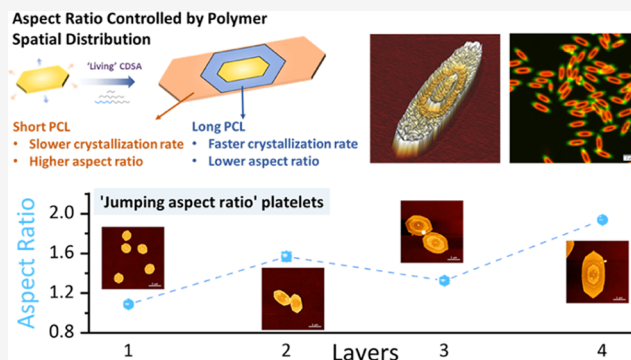


Article Recommendations



Supporting Information

**ABSTRACT:** The aspect ratios of nano- and micrometer-sized features in nature have evolved to enable specific characteristics that are finely tuned for optimizing strength, surface area, optics, and heat dissipation. Despite the importance of aspect ratios, precise control over the aspect ratios of anisotropic polymeric nanoparticles is challenging to achieve and the formation mechanisms by which they occur are not fully understood. In this study, using the crystallization-driven self-assembly (CDSA) process, we achieved two-dimensional (2D) platelets with precisely controlled aspect ratios through the rational compositional adjustment of various polycaprolactone (PCL)-based homopolymers (HP) and block copolymers (BCP). These polymer compositions exhibit distinct polymer crystallization rates, which allow for highly controlled aspect ratios and polymer spatial distribution in 2D platelets. Brownian dynamics (BD) simulations provided an in-depth understanding of the formation of 2D platelets. The BD simulations help us further confirm the nature of living epitaxial growth, simulate the structural order of polymer chains during the CDSA process, and demonstrate the influence of PCL length on the aspect ratio. Our work opens up new possibilities for a nuanced understanding of the interplay between polymer composition, crystallization rate, and morphology, providing a method for the controlled synthesis of 2D nanostructures.



## INTRODUCTION

Throughout nature, numerous examples highlight the importance of the aspect ratio of materials to their efficient function, as different aspect ratios exhibit different functions under different circumstances. For instance, honeybee hives adopt a low aspect ratio to maximize honey storage while minimizing wax usage.<sup>1,2</sup> Conversely, the intricate branching patterns of trees governed by a long aspect ratio provide a larger surface area for improved nutrient transport.<sup>3</sup> It is logical to expect that the aspect ratio of polymeric material structures would also be important in directing performance; however, their study has been frustrated due to the limited synthetic methodology used to access such structures. Hence, inspired by these natural phenomena, we have sought to design new synthetic materials with precisely controlled aspect ratios that will enable optimization of their properties in future applications.

Crystallization-driven self-assembly (CDSA) provides a promising method to prepare nanoscale anisotropic particles.<sup>4–6</sup> This approach utilizes a crystallizable core-forming block, stabilized by a solvophilic corona block, to form uniform nanostructures with controlled size, morphology, and dimensions.<sup>7–22</sup> Despite these advancements, the mechanism of self-assembly for anisotropic nanostructures remains poorly

understood, with limited studies focused on regulating the aspect ratio of CDSA assemblies.<sup>23–26</sup> In CDSA, the aspect ratio of the resulting nanostructures is influenced by various factors such as temperature, solvent, polymer topology, and properties of the monomers involved.<sup>27–31</sup> Despite the complexity introduced by these factors, previous research indicates that a common factor plays a central role in determining the aspect ratio: the rate of crystallization. When molecules undergo self-assembly driven by crystallization, they tend to organize themselves into ordered structures to minimize free energy.<sup>32</sup> A difference in the crystallization rate between different directions and crystalline planes within the structure can lead to the formation of elongated or anisotropic nanostructures with specific aspect ratios.<sup>33</sup> This difference in crystallization rates may arise due to factors such as molecular packing efficiency, orientation of crystalline domains, or differences in surface energies along different

**Received:** October 13, 2024

**Revised:** November 14, 2024

**Accepted:** November 18, 2024

**Published:** November 29, 2024



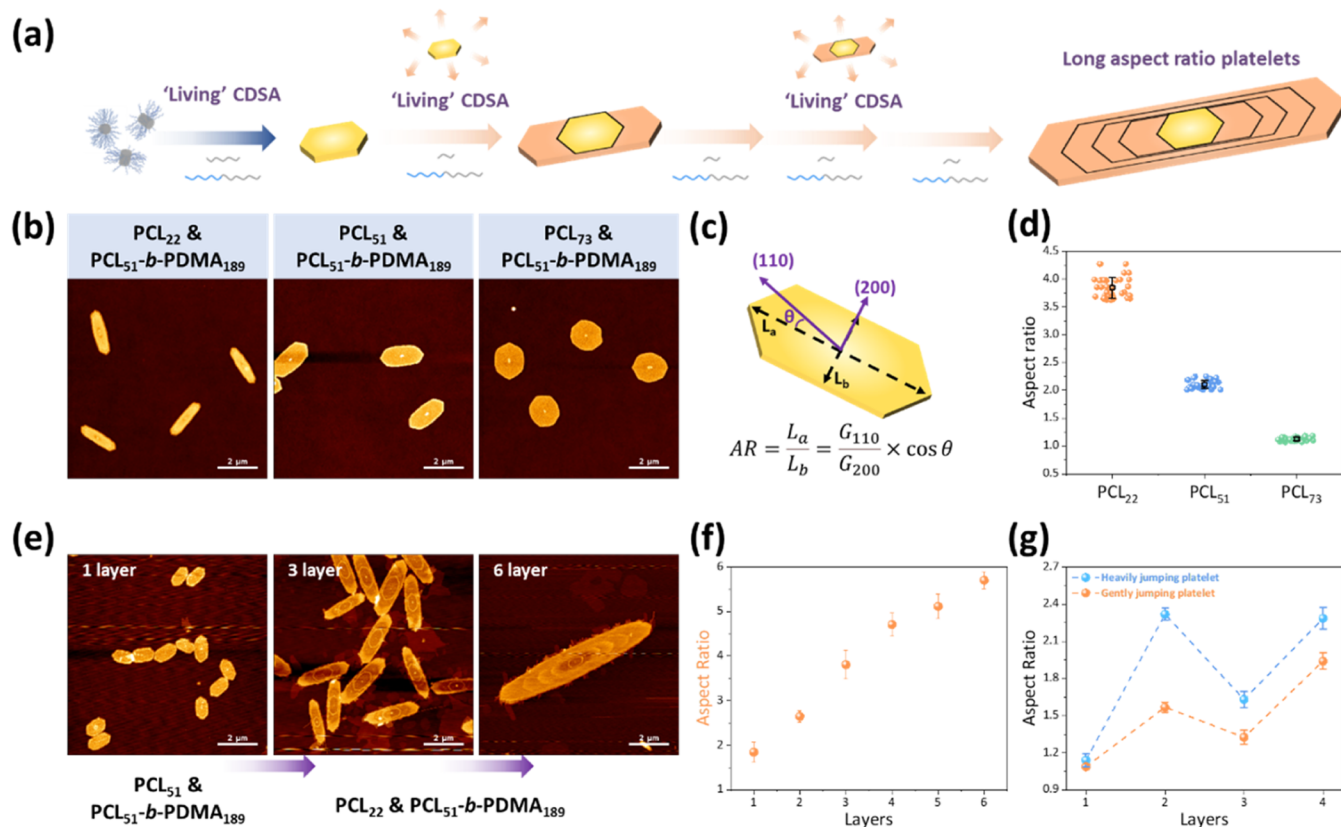


**Figure 1.** Controlling aspect ratio by varying the PCL length. (a) Schematic representation of the preparation of long aspect ratio multilayered platelets by living CDSA. (b) Platelets formed using different lengths of PCL homopolymers (PCL<sub>22</sub>, PCL<sub>51</sub>, PCL<sub>73</sub>) with fixed block copolymers of PCL<sub>51</sub>-*b*-PDMA<sub>189</sub> prepared by living CDSA, scale bar = 2 μm (utilizing PCL<sub>51</sub>-*b*-PDMA<sub>189</sub> seed solution of 0.01 mg/mL in ethanol). (c) Illustration highlighting the aspect ratio of the platelets. (d) Plots depicting the aspect ratio of different PCL length platelets. (e) AFM images of long aspect ratio platelets (first layer platelet composed of PCL<sub>51</sub>/PCL<sub>51</sub>-*b*-PDMA<sub>189</sub>, and then further growing layers using unimer of PCL<sub>22</sub>/PCL<sub>51</sub>-*b*-PDMA<sub>189</sub> via living CDSA). (f) Plots depicting the aspect ratio of long aspect ratio platelets. (g) "Jumping aspect ratio" platelets, in which the 1st and 3rd layers are composed of PCL<sub>73</sub>/PCL<sub>51</sub>-*b*-PDMA<sub>189</sub>, while the 2nd and 4th layers are composed of PCL<sub>22</sub>/PCL<sub>51</sub>-*b*-PDMA<sub>189</sub>.

crystallographic directions.<sup>34–36</sup> Understanding the underlying mechanisms behind these differences can lead to the development of strategies for precisely tuning the aspect ratios of nanostructures. This could open up new possibilities for engineering nanomaterials with tailored properties for a wide range of applications, from drug delivery to photonics.<sup>37–39</sup>

Some advances have been made toward these goals; for example, Choi's group observed a change in shape from square to rectangular with an increasing aspect ratio when solvents such as tetrahydrofuran or chloroform were added to the solution of conjugated poly(cyclopentylene-vinylene) (PCPV)-based polymer. This change was attributed to the differences in surface energy and crystallization rate among three crystalline planes ((110) > (010) > (100)).<sup>40</sup> Additionally, Tang and co-workers reported that increasing the length of the charged corona block could decrease the aspect ratio of platelets. The aspect ratio of polycaprolactone-*b*-poly(cobaltocenium amidoethyl methacrylate) (PCL-*b*-PCoAEMA) platelets was influenced by the electrostatic repulsion between chains, resulting in the distinct crystallization rate in longitudinal and lateral directions.<sup>41</sup> Further development of our fundamental understanding of these noncovalent interactions remains essential to precisely control the particle aspect ratio over a larger range of copolymer structures, for example with charged units, to enable advances in materials

technologies where these structures may be important, such as biomedicine and microelectronics.<sup>42–44</sup>

Herein, we present a simple strategy to create two-dimensional (2D) platelets with controlled aspect ratios and polymer spatial distributions via living CDSA. By varying the core and corona length, we can modulate the crystallization rate of polymer chains to fold them in an orderly fashion to form platelets. This work establishes the relationship between polymer composition and crystallization rate to better understand the living CDSA process and achieve the resulting nanostructures with tunable aspect ratios and polymer spatial distribution.

## RESULTS AND DISCUSSION

**Polymer Synthesis and Seed Preparation.** 2D platelets were normally fabricated using a 1:1 wt % ratio of homopolymer (HP) and block copolymer (BCP). In this study, poly( $\epsilon$ -caprolactone) (PCL) was utilized as the semicrystalline core-forming block, while poly(*N,N*-dimethylacrylamide) (PDMA) served as the solvophilic stabilizing corona block.<sup>45,46</sup> PCL was selected due to its biodegradability and biocompatibility, rendering it a promising candidate for a variety of biological applications. To investigate the influence of polymer chain length on crystallization, three PCL<sub>*n*</sub> homopolymers ( $n = 22, 51, 73$ ) and 12 PCL<sub>*n*</sub>-*b*-PDMA<sub>*m*</sub> block copolymers ( $n = 22, 51, 73; m =$  approximately 50,

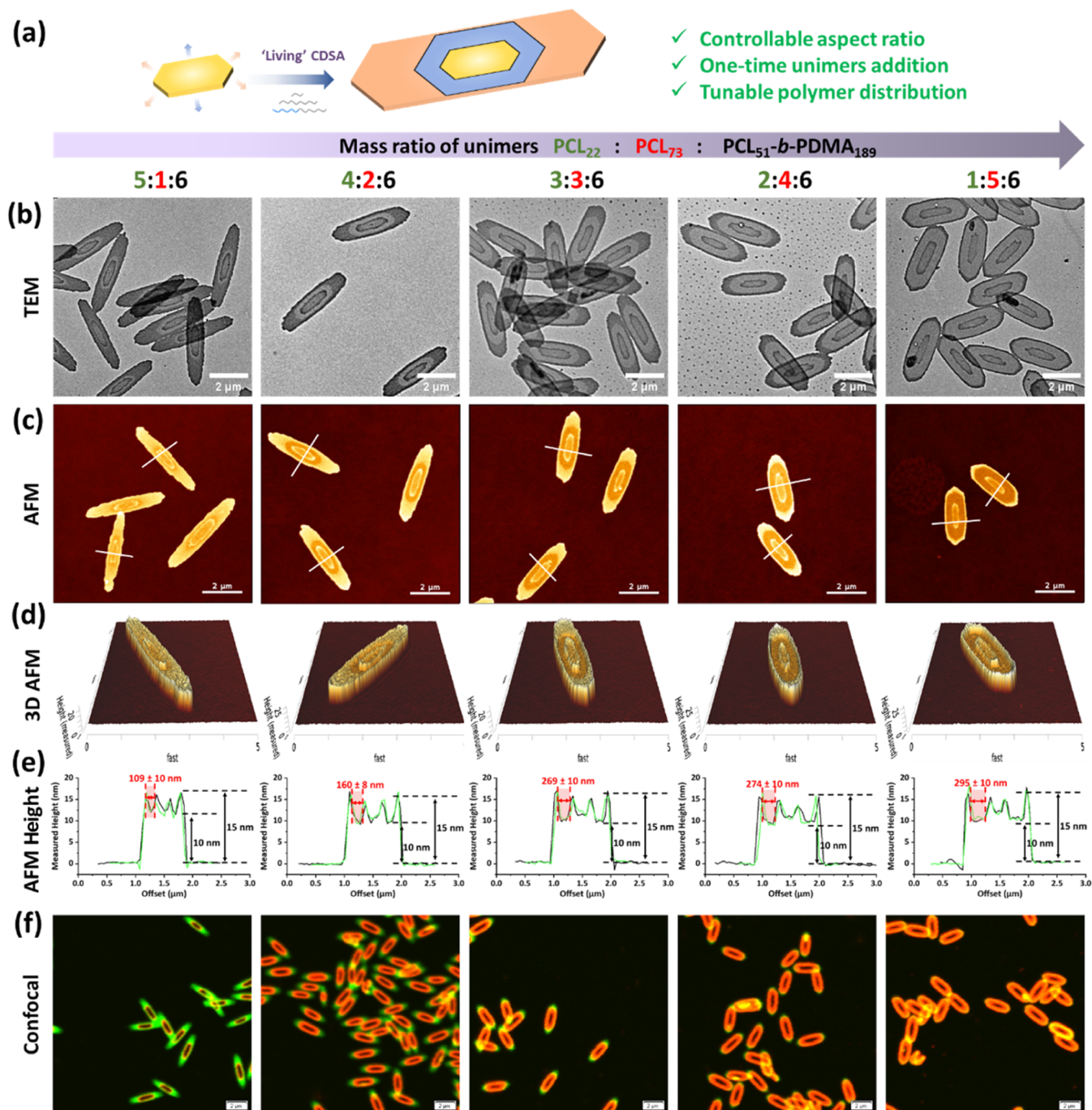


**Figure 2.** Mixed long/short PCL for regulating platelets shape. (a) Schematic representation of the fabrication of 2D platelets. (b) TEM, (c) AFM, (d) 3D AFM, (e) AFM height profile, and (f) confocal images of 2D platelets consisting of different ratios of long and short PCL (PCL<sub>22</sub> and PCL<sub>73</sub>) with a fixed amount of block copolymers PCL<sub>51</sub>-*b*-PDMA<sub>189</sub>. (For confocal characterization, borondipyrromethene (BODIPY) dye-modified short and long PCL (PCL<sub>22</sub>-FL and PCL<sub>73</sub>-630/650) were utilized.)

100, 200, 300) were synthesized following previously reported procedures.<sup>45</sup> The molecular weights and dispersities of all polymers were confirmed by <sup>1</sup>H NMR spectroscopy and size exclusion chromatography (SEC) (Scheme S1, Figures S1–S22, and Table S1). Prenucleated seeds of PCL-*b*-PDMA were prepared via a two-step process: the self-assembly of PCL<sub>51</sub>-*b*-PDMA<sub>189</sub> into cylinders of varying lengths in ethanol, followed by the sonication of the resulting cylinder into short rods (Figure S23). These seeds served as the nuclei from which further crystallization was able to present uniform growth on the seed surface (living CDSA). Here, various polymer blends

of PCL<sub>*n*</sub> and PCL<sub>*n*</sub>-*b*-PDMA<sub>*m*</sub> were used to fabricate platelets by living CDSA (see the Supporting Information for experimental details).

**Precise Modulating Aspect Ratio of Platelets.** To elucidate the impact of core length on crystallization behavior, different length PCL (DP = 22, 51, 73) were synthesized, and their basic physicochemical properties have been characterized. X-ray diffraction (XRD) analysis was conducted to determine the crystallization parameters. Comparing the relative intensity between crystalline peak (110) and (200), it was found that the intensity of crystalline peak (110) increased with

decreasing PCL length (Figure S24). Furthermore, non-isothermal differential scanning calorimetry (DSC) was conducted under bulk conditions, showing that the crystallization and melting temperatures rose with increasing PCL length (DP = 22, 51, 73), from 31.2 to 40.0 and 49.1 to 56.0 °C, respectively (Figure S25 and Table S2). Analysis of the melting enthalpy revealed that crystallinity ( $X_c$ ) exhibited a bell-shaped curve, with the maximum  $X_c$  observed at an optimal PCL length of DP = 22 (Figure S26). The subsequent decrease in crystallinity with increasing PCL length was attributed to a reduction in chain diffusion accompanied by an increase in entanglement density.<sup>47</sup> After confirming basic physicochemical characteristics, various lengths of PCL (DP = 22, 51, 73) with fixed block copolymers of PCL<sub>51</sub>-*b*-PDMA<sub>189</sub> were utilized to fabricate platelets via living CDSA. The observed aspect ratios of the platelets varied between 1 and 4 across different PCL chain lengths (Figures 1b–1d and S27), indicating that PCL length significantly influences the aspect ratio of 2D CDSA platelets.

When HPs of PCL<sub>22</sub> were employed instead of PCL<sub>51</sub> for seeded growth, an augmentation in platelet aspect ratio was observed. Notably, following successive unimer additions, the aspect ratio increased from 1.8 to 6 (Figures 1a, 1e, 1f, S28, and S29). Platelets exhibited a preference for elongated growth along the length (long axis) as opposed to the width (short axis), leading to an increased aspect ratio. However, in a previous study, multilayered platelets composed of a PCL<sub>50</sub>-based polymer were obtained by epitaxial growth, where different layers maintained a similar shape and aspect ratio.<sup>45</sup> Given the distinct aspect ratios associated with different PCL lengths, an adjustable platelet shape was demonstrated through the preparation of “jumping aspect ratio” platelets, in which “heavily jumping platelets” exhibited undulating transitions from 1.1 to 2.3 and then to 1.6, and subsequently to 2.3 (Figures 1g and S30). These were achieved by living CDSA employing an odd layer composed of PCL<sub>73</sub>/PCL<sub>51</sub>-*b*-PDMA<sub>189</sub> and an even layer composed of PCL<sub>22</sub>/PCL<sub>51</sub>-*b*-PDMA<sub>189</sub>.

The results demonstrate that the platelet aspect ratio is higher when the PCL length is shorter, resulting in a more slender crystal shape. This relationship between the PCL length and platelet aspect ratio needs further clarification. This alteration in the platelet aspect ratio may arise from differing crystallization rates from different crystalline facets. Hence, preferential growth from different orientations along specific crystalline planes could be used to alter the aspect ratio by varying the crystallization rate in this manner.<sup>48</sup> The increased aspect ratio has been linked in previous reports to the shifting relative crystallization rates of each crystal plane of (110) and (200) as the experimental crystallization temperature ( $T_{ec}$ ) rises.<sup>27,48,49</sup> However, in this case, with a fixed  $T_{ec}$  (20 °C), the platelet aspect ratio is higher when the PCL length is shorter, corresponding to a more slender crystal shape. This suggests that the aspect ratio is not exclusively determined by  $T_{ec}$ . Potential explanation, rooted in polymer crystal growth theory,<sup>50,51</sup> is that the aspect ratio correlates with  $\phi$ , a parameter dependent on supercooling ( $\Delta T$ , defined as  $T_m^0 - T_{ec}$ , where  $T_m^0$  represents the equilibrium melting temperature and  $T_{ec}$  is the experimental crystallization temperature).  $\phi$  denotes the fraction of the forward and backward reaction rate of the polymer chains' crystallographic attachment. Due to the partial exclusion effect, certain PCL chain units may be excluded from the crystalline domain and accumulate on the

folding surface, thereby altering the energy required for chain folding. Consequently, the efficiency of converting from coil to crystal decreases, resulting in a decrease in  $\phi$ , which may elucidate the more slender shape observed in platelets comprising shorter PCL chains. Similar to polyethylene (PE) crystallization from dilute solutions,<sup>52</sup> as the degree of supercooling decreases, there is a transition from regular lozenge-type single crystals with predominantly (110) outer planes to truncated crystals that also exhibit (100) planes. PCL possesses orthorhombic unit cells similar to those of PE, indicating structural similarities that influence their crystallization behavior under different supercooling conditions.

#### Mixed Long/Short PCL Modulating Platelets Shape.

Following the identification of the impact of PCL length on the aspect ratio, a hybrid system comprising a blend of short and long PCL (with fixed BCP content) was investigated to attain a higher level of control. Specifically, blending unimers consisting of PCL<sub>22</sub>/PCL<sub>73</sub>/PCL<sub>51</sub>-*b*-PDMA<sub>189</sub> were selected to validate this hypothesis, with the mass ratio of PCL<sub>n</sub> HPs and PCL<sub>51</sub>-*b*-PDMA<sub>189</sub> BCPs fixed at 1:1 (w/w), and only the mass ratio of PCL<sub>22</sub> to PCL<sub>73</sub> varying. TEM and AFM analyses revealed a predictable decrease in the aspect ratio with an increase in the proportion of long PCL (PCL<sub>73</sub>), transitioning from elongated platelets to bloated platelets with an aspect ratio ranging from 6.5 to 1.8 (Figures 2a–c, S31, and S32). Intriguingly, besides the original inner layer of “platelet seeds,” two additional layers were discerned following the addition of blending unimer. With an increase in the content of PCL<sub>73</sub> and a corresponding reduction in PCL<sub>22</sub>, the area (and width) of the middle layer expanded while that of the outer layer contracted (Figure 2b–2e). Based on the observed alterations in area (also including length and width) under differing content levels, it was inferred that the middle and outer layers corresponded to the PCL<sub>73</sub> and PCL<sub>22</sub> layer, respectively. Another noteworthy phenomenon is the difference in the thickness of the PCL crystal layers observed in AFM height profiles and three-dimensional (3D) AFM images. This difference matches the variation in the layer contrast observed in TEM images (Figure 2b). This extra height is possibly caused by the distribution of BCP, assuming that the crystallization rate of PCL<sub>22</sub> and PCL<sub>51</sub>-*b*-PDMA<sub>189</sub> is similar, resulting in the thick PCL<sub>22</sub> layer. To further confirm this observation, the height profiles of pure PCL<sub>n</sub> platelets ( $n = 22, 51, 73$ ) and PCL<sub>n</sub>/PCL<sub>51</sub>-*b*-PDMA<sub>189</sub> platelets were analyzed and compared using AFM (Figures S33 and S34). Pure PCL platelets (without block copolymer PCL-*b*-PDMA) exhibited a flat height profile with a thickness of approximately 9–10 nm. Pure PCL platelets exhibited distinct aspect ratios across different PCL chain lengths, following a trend similar to that observed in PCL<sub>n</sub>/PCL-*b*-PDMA platelets. PCL crystallizes in an orthorhombic unit cell with lattice parameters  $a = 0.748$  nm,  $b = 0.498$  nm, and  $c = 1.726$  nm. The space group is  $P2_12_12_1$ , and the polymer chain adopts a 7/2 helix conformation.<sup>53</sup> The calculation based on the crystallographic unit cell indicates that, depending on the degree of polymerization (DP) of the PCL chains (DP = 22, 51, 73), the chains fold 1, 4, and 6 times, respectively, to achieve this thickness.<sup>27</sup> The folding occurs because PCL chains align and crystallize in a lamellar fashion with the folded chains being the kinetically stable chain conformation to produce fast crystallization. In the PCL<sub>n</sub>/PCL<sub>51</sub>-*b*-PDMA<sub>189</sub> platelet system, for  $n = 51$  and 73, the center height was around 10 nm, with the edge reaching about 15 nm (Figure S35). This difference

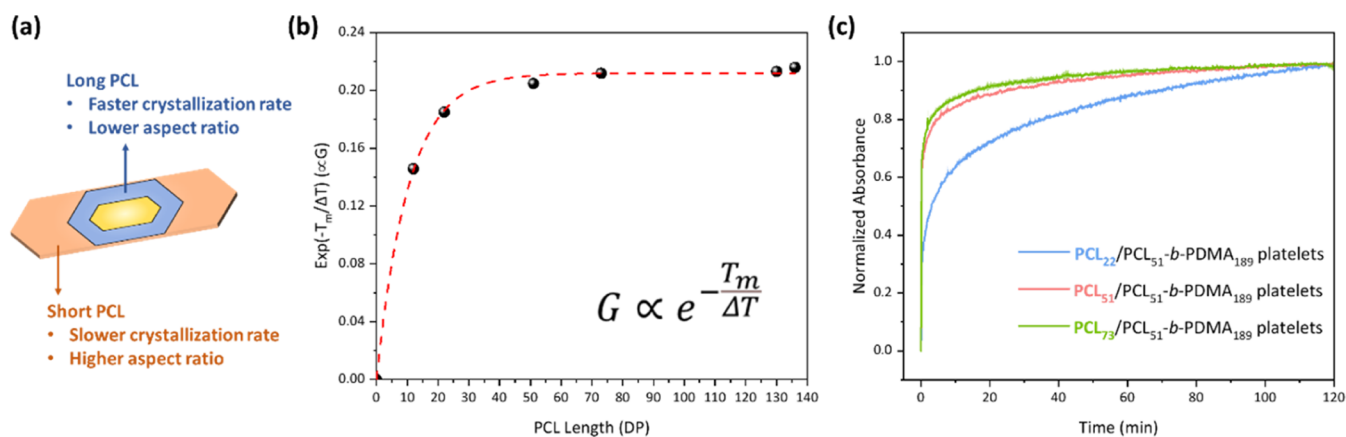


**Figure 3.** Crystallization rate of different length PCL. (a) Illustration highlighting crystallization and morphology behavior of different PCL lengths for 2D platelets. (b) Relationship between PCL length and crystallization rate according to Lauritzen–Hoffman (LH) growth theory. (c) CDSA kinetics by tracking changes in UV–vis absorbance (500 nm) over time when adding  $\text{PCL}_n/\text{PCL}_n\text{-}b\text{-PDMA}_m$  unimer solutions to seed solutions.

occurs because the crystallization rate of  $\text{PCL}_{51}$  and  $\text{PCL}_{73}$  is significantly faster than that of  $\text{PCL}_{51}\text{-}b\text{-PDMA}_{189}$ . When  $n = 22$ , the platelets also displayed a flat height profile of approximately 15 nm. These results confirmed that the pure PCL crystalline layer has a thickness of approximately 9–10 nm, with the additional height attributed to the block copolymer corona. This can be attributed to the similar crystallization rates of  $\text{PCL}_{22}$  and  $\text{PCL}_{51}\text{-}b\text{-PDMA}_{189}$ , which led to a uniform distribution across platelets. Furthermore, the similar crystallization rates of  $\text{PCL}_{22}$  and  $\text{PCL}_{51}\text{-}b\text{-PDMA}_{189}$  were later confirmed by in situ UV–vis observations.

To further prove the spatial distribution of polymer, different length PCL HPs have been end-group modified with various borondipyromethene (BODIPY) fluorophores that possess distinct emission channels (see experimental details in SI, Scheme S2). SEC coupled with ultraviolet (UV) absorbance detection showed successful fluorescent dye attachment, meanwhile PCL molecular weights and narrow dispersities ( $\mathcal{D}_M < 1.11$ ) were well maintained (Figures S36–S38 and Table S3). From the confocal images, short-length  $\text{PCL}_{22}$  with green fluorescence mainly distributes on the outer layer of platelets, while long-length  $\text{PCL}_{73}$  with red fluorescence is located on the middle layer (Figures 2f and S39). With a change in the short and long PCL ratios, the area of fluorescence changed. When using  $\text{PCL}_{51}$  instead of  $\text{PCL}_{73}$ , a similar phenomenon was observed (Figures S40 and S41). This indicates that the crystallization rate of longer PCL ( $\text{PCL}_{73}$  and  $\text{PCL}_{51}$ ) is faster compared to shorter PCL ( $\text{PCL}_{22}$ ). Additionally, the longer PCL results in platelets with shorter aspect ratios. Therefore, it may be inferred that the crystallization rate of PCL may influence the aspect ratio. To elucidate the correlation between crystallization rate and aspect ratio, two distinct concentration regimes were employed for living CDSA: unimer solutions at 10 and 50 mg/mL and seed solutions at 0.01 and 0.05 mg/mL. The above solutions were chosen as higher concentrations led to an accelerated crystallization process. Under higher concentration conditions, platelets displayed reduced aspect ratios across the three PCL chain lengths investigated (Figures S42 and S43). This observation underscores the concentration-dependent (crystallization rate) effect on the aspect ratio during the CDSA process. Higher concentrations, associated with a faster crystallization rate, tend to form platelets with reduced aspect ratios. Next, the relationship between PCL length, crystal-

lization rate, and aspect ratio of the assemblies will be investigated in more detail.

**Relationship between the PCL Chain Length and Crystallization Rate.** According to the Lauritzen–Hoffman (LH) growth theory,<sup>33,54</sup> the living CDSA method offers ample seeds that serve as nuclei for further spread (lateral) growth, thereby avoiding uncontrollable self-nucleation. The growth rate ( $G$ ) can be described by the equation

$$G = e^{-4l\sigma_p\sigma_f T_m/k\Delta h_f^{\text{eq}} T_{\text{cc}}\Delta T} \propto e^{-T_m/\Delta T} \quad (1)$$

where  $l$  represents the platelet thickness (stem length);  $\sigma_p$  is the platelet surface free energy;  $\sigma_f$  is the fold surface free energy;  $k$  is the Boltzmann constant;  $\Delta h_f^{\text{eq}}$  is the equilibrium fusion (melting) enthalpy or the melting of a PCL sample with 100% crystallinity; and  $T_{\text{cc}}$  is the experimental crystallization temperature (also the actual crystallization temperature). In this case,  $T_m$  or the experimentally determined melting temperature has been employed. In the original equation,  $\Delta T$  is the thermodynamic supercooling, equal to  $T_m^{\circ} - T_{\text{cc}}$ . In this work, an experimental approximate value of supercooling was employed using  $T_m$  instead of  $T_m^{\circ}$ . For further confirmation, a  $T_m^{\circ}$  value reported in the literature has been employed for the calculation,<sup>47</sup> showing the same trend (Figures S44, S45, and Table S4). According to eq 1, the growth rate ( $G$ ) is inversely proportional to the value of  $T_m/\Delta T$  (where  $T_m/\Delta T = T_m/(T_m - T_{\text{cc}})$ ). Since the melting temperature ( $T_m$ ) varies with the length of PCL chains in the low molecular weight range (particularly below 5 kg/mol), the differences in crystallization rates can be caused by the PCL lengths. The results indicate that longer PCL chains exhibit a smaller  $T_m/\Delta T$  with a faster crystallization rate (Figure 3a,3b and Table S4), which is consistent with the AFM, TEM, and confocal microscopy results, clarifying the interplay between the PCL length and crystallization rate.

Additionally, UV–vis spectroscopy was employed to monitor the crystallization rates by tracking changes in absorbance over time to elucidate the influence of PCL chain length on the self-assembly kinetics.<sup>18</sup> To clarify, the wavelength of 500 nm was chosen for monitoring absorbance changes over time, as the absorbance trithiocarbonate group of the CTA is located at 309 nm. To avoid interference from this specific absorbance and instead focus on the assembly evolution (e.g., changes in size and area), we selected 500 nm as a representative wavelength, where changes in scattering

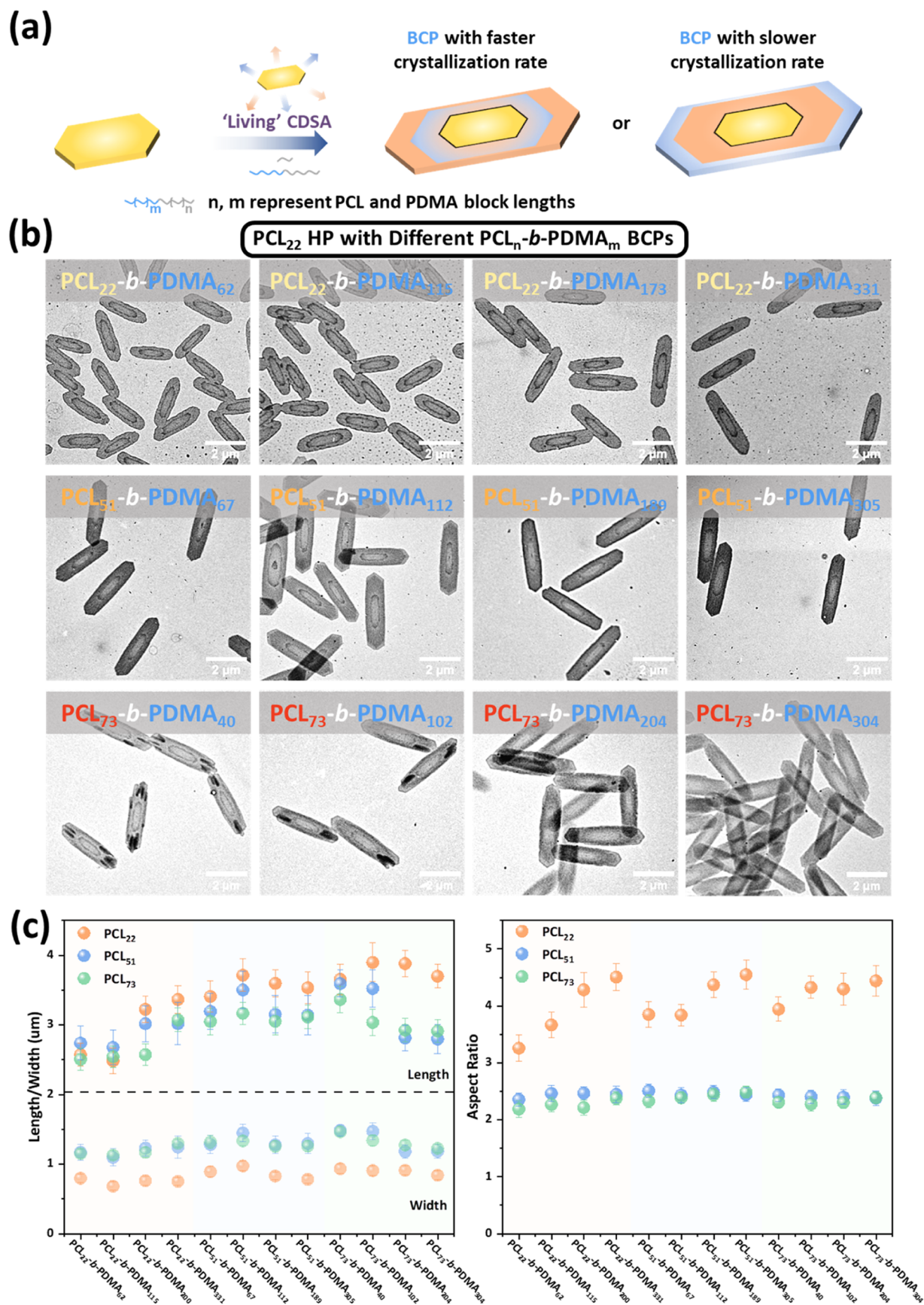


**Figure 4.** Simultaneous effect of PCL<sub>22</sub> HP and different PCL<sub>n</sub>-*b*-PDMA<sub>m</sub> BCPs for yielding 2D platelets. (a) Preparation route of 2D platelets from 12 different kinds of PCL-*b*-PDMA with fixed PCL via living CDSA. (b) TEM images of 2D platelets encompassing different core and corona lengths of BCPs PCL<sub>n</sub>-*b*-PDMA<sub>m</sub> with fixed PCL<sub>22</sub> HPs via living CDSA. (c) Length, width, and aspect ratio plots of 2D platelets encompassing different core and corona lengths BCPs PCL<sub>n</sub>-*b*-PDMA<sub>m</sub> with different HPs via living CDSA.

and absorbance occur as the assemblies form and grow. Upon adding  $\text{PCL}_n/\text{PCL}_n\text{-}b\text{-PDMA}_m$  unimer solutions to seed solutions, absorbance at 500 nm exhibited an initial increase followed by stabilization (Figures 3c and S46). For longer PCL systems, the absorbance peaked within several minutes and remained stable thereafter, whereas shorter PCL systems displayed a delayed peak. Concurrently, the Tyndall effect was assessed by irradiating the samples with a green laser (around 560 nm) at different time points (2 and 60 min, Figure S47). For the short PCL system in the living CDSA process, the light beam intensity was initially weak at 2 min but intensified to levels comparable to the long PCL system by 60 min. In contrast, the light beam intensity for the long PCL system remained consistent over the same period. These observations align with the UV-vis data, suggesting that longer PCL chains facilitate a rapid self-assembly process characterized by a high crystallization rate. In contrast, shorter PCL chains exhibit a slower crystallization rate, indicating a slower CDSA process. Furthermore, as previously mentioned, the crystallization rates of  $\text{PCL}_{22}$  and  $\text{PCL}_{51}\text{-}b\text{-PDMA}_{189}$  are comparable (Figure 2). In situ UV-vis observation was employed to investigate the platelet formation process at different mass ratios of  $\text{PCL}_{22}$  and  $\text{PCL}_{51}\text{-}b\text{-PDMA}_{189}$  (2:1, 1:1, and 1:2, Figures S48 and S49). The resulting absorbance curves are nearly identical, confirming similar crystallization rates of  $\text{PCL}_{22}$  and  $\text{PCL}_{51}\text{-}b\text{-PDMA}_{189}$ .

The results indicated that PCL length significantly influences the crystallization rate, leading to 2D CDSA platelets with varying aspect ratios. We hypothesize that the observed changes in aspect ratio are due to the impact of crystallization kinetics on the crystallization rates of different crystalline planes of the (110) and (200).<sup>53,55</sup> The (200) plane with a higher Miller index has higher surface energy, while the (110) plane is denser and has lower surface energy, promoting anisotropic growth, particularly when the crystallization rate is slower.<sup>56</sup> For longer PCL chains, the faster crystallization rate provides sufficient energy to overcome the energy barriers associated with both planes more uniformly. This results in more symmetrical growth, yielding platelets with lower aspect ratios. Conversely, shorter PCL chains crystallize more slowly, leading to insufficient energy to uniformly overcome the barriers across all planes. This favors the growth of the lower surface energy (110) plane, resulting in a more anisotropic growth. Consequently, the platelets exhibit higher aspect ratios, with the structure elongating more significantly in one direction. This explains the relationship between the crystallization rate and the aspect ratio of the resulting nanostructures.

**Simultaneous Influence of HPs and BCPs for 2D Platelets.** To deepen our understanding of the crystallization rate of polymers (HPs and BCPs) and its impact on self-assembly behavior, various combinations of HPs and BCPs with different core and corona lengths were employed for living CDSA. A series of unimer solutions, comprising 3 kinds of HPs and 12 varieties of BCPs (resulting in 36 permutations), were introduced into the “platelets seeds” solution (“platelets seeds” information in Figure S50) to fabricate 2D platelets via living CDSA. A “phase” diagram was constructed to represent the morphology and polymer spatial distribution under different HP and BCP combinations (Figure 4). When short-length  $\text{PCL}_{22}$  was used as HP, compared to the original “platelet seeds,” there was a slight increase in width, ranging from approximately 0.7 to 0.9  $\mu\text{m}$ , and the aspect ratio

exceeded 3.5 (Figure 4a–4c). Interestingly, TEM characterization revealed differences in polymer spatial distribution (location) within specific regions, even with some samples displaying defects on the platelets, which may be attributed to the significant difference in the crystallization rate between  $\text{PCL}_{22}$  HP and various BCPs. This difference could potentially result in diverse polymer folding behavior and optimal crystallization orientations from specific crystalline planes. To further investigate whether these platelets or defects form during the living CDSA process, dynamic light scattering (DLS) analysis was performed on unimer solutions of  $\text{PCL}_{22}$ ,  $\text{PCL}_{51}$ ,  $\text{PCL}_{73}$ ,  $\text{PCL}_{51}\text{-}b\text{-PDMA}_{189}$ , and pure solvent. The size measurements obtained were all below 10 nm (Figure S51), which is below the detection limit of the DLS technique. This suggests that the polymers are fully dispersed in the solvent, existing in an individual unimer state rather than as aggregates prior to crystallization. This observation supports the hypothesis that the platelets and defects observed originate during the crystallization process rather than from pre-existing polymer aggregates.

However, compared to the short PCL ( $\text{PCL}_{22}$ ) system, a distinct phenomenon was observed when long PCL HPs (with a DP of 51 or 73) were combined with various BCPs: the morphology exhibited minimal variation (Figures S52 and S53). The dimensions, including length and width, ranged from approximately 2.8 to 3.2 and 1.1 to 1.3  $\mu\text{m}$ , respectively, resulting in an aspect ratio of 2.2–2.4 (Figure 4c). Additionally, the polymer spatial distribution maintained a consistent pattern with BCP primarily distributed along the boundary/edge of platelets. This behavior is attributed to the relatively faster crystallization rate of the long HPs ( $\text{PCL}_{51}$  and  $\text{PCL}_{73}$ ) compared to the BCPs. Since the platelet seeds possessed sufficient active sites for epitaxial growth, the faster crystallization process did not result in significant morphological differences.

To further elucidate the spatial distribution of the block copolymer ( $\text{PCL}\text{-}b\text{-PDMA}$ ), a mixture of unimers of various  $\text{PCL}\text{-}b\text{-PDMA}$  and homopolymers ( $\text{PCL}_{22}$  and  $\text{PCL}_{73}$ , in a 2/1/1 w/w/w) was added into a seed solution for living CDSA. TEM and AFM imaging with a height profile (Figures S54 and S55) revealed variations in the height and spatial distribution of the platelets. These differences indicate the impact of polymer composition on crystallization rates and the resulting morphological outcomes of the platelets, confirming that the spatial arrangement of block copolymers, influenced by their distinct crystallization kinetics, plays a crucial role in determining the overall structure of the assemblies. This approach offers a straightforward method to achieve “self-lithography” in micro- and nanostructures, with potential applications in microelectronic circuits and localized environmental channels.

**Computational Simulation for Crystallization Behavior during the CDSA Process.** While experimental findings underscore the significance of the core and corona length of homopolymers (HPs) and block copolymers (BCPs) in crystallization behavior, obtaining detailed insights solely from experiments is challenging. Brownian dynamics (BD) simulations were conducted to deepen our understanding of the growth behavior and to further confirm proposed hypotheses regarding the controllable crystallization kinetics governing the formation of self-assembled platelets.<sup>57–59</sup> Two main aspects were investigated: first, the influence of the PCL length on the platelet’s aspect ratio, and second, the evolution

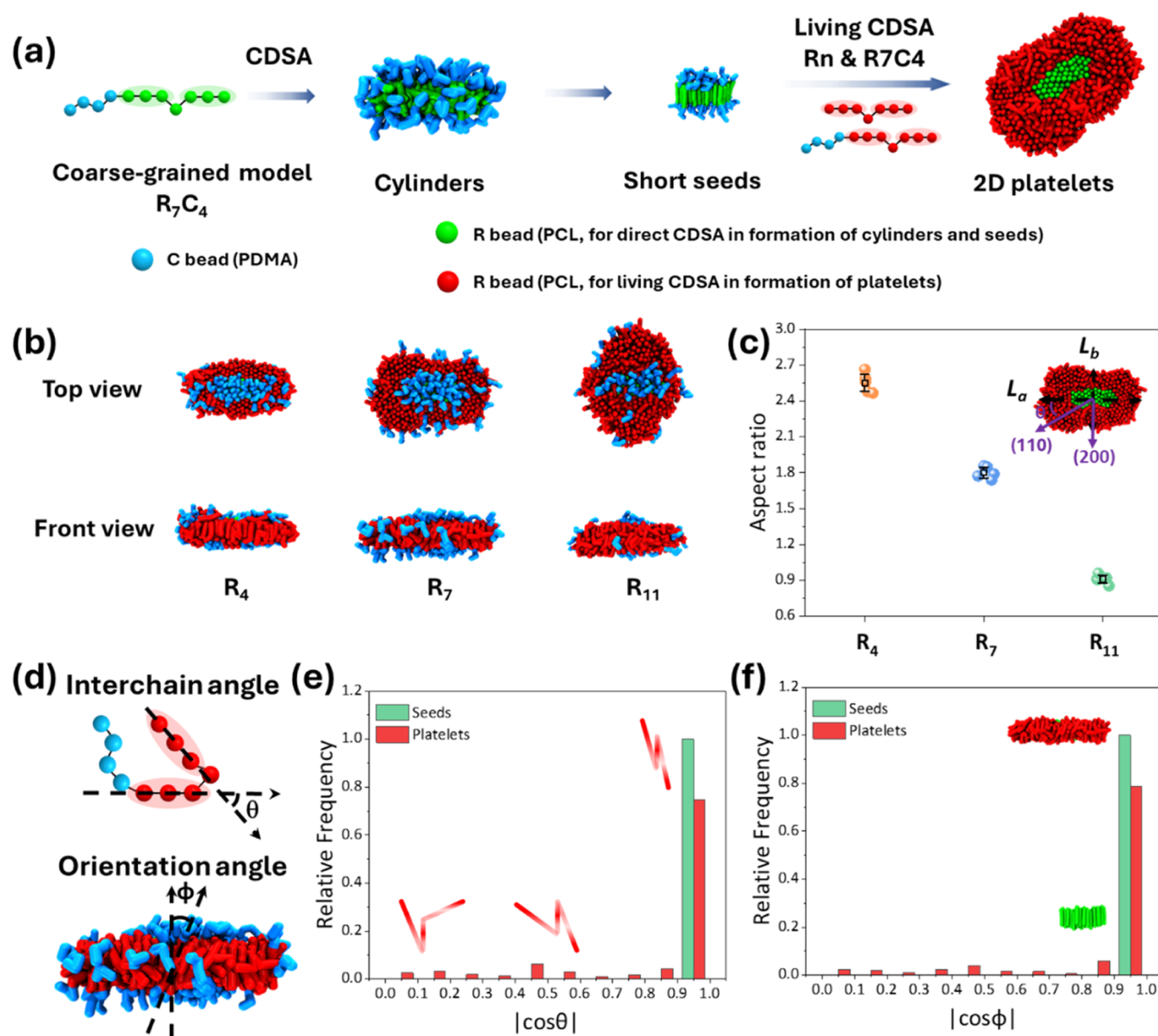


**Figure 5.** Living CDSA of 2D platelets by Brownian dynamics (BD) simulation. (a) Schematic representation of the BD simulation pathway for preparing 2D platelets utilizing a coarse-grained model. (b) Simulated morphology images (top view and front view) of 2D platelets obtained using different lengths of PCL homopolymers ( $R_4$ ,  $R_7$ ,  $R_{11}$ ) with fixed PCL-*b*-PDMA block copolymers of  $R_7C_4$ . (c) Plots depicting the aspect ratio of 2D platelets with different PCL lengths determined by BD simulation. (d) Diagram illustrating the interchain angle within a single polymer chain and the orientation angle between PCL chains and the axis perpendicular to the central axis of the platelets. (e) Relative frequency plots of the interchain angle (absolute value of  $\cos \theta$ ) illustrating the local order of individual polymer chains. Insets depict the schematic representation of varying folding angles within the polymer chains. (f) Relative frequency plots of the orientation angle (absolute value of  $\cos \phi$ ), demonstrating the overall order of polymer chain folding in 2D platelets. Insets show the front view of seeds (green) and platelets (red) to indicate the orientation angle of polymer chain folding and the normal vector direction of the platelets.

of order of PCL-based polymer chains during the CDSA process. The simulation process utilized a coarse-grained model composed of two types of beads (Figure S56): a crystalline core of PCL ( $R_m$  beads) and a hydrophilic corona of PDMA ( $C_n$  beads, subscript denotes the bead number, other settings of models and simulation parameters detailed in SI). The order and folding manner of PCL HPs during the crystallization process were achieved by setting the alternating rigid and flexible bond angles along the  $R_m$  bead–spring chains and the attractive interaction potentials between R–R beads to describe the crystallization effect of PCL. Initially, under the condition of an interaction strength  $\epsilon_{RR}$  of 3.0 (other

parameters detailed in SI), cylinders were formed by the direct CDSA of the  $R_7C_4$  block copolymer, and the process of cylinder formation is illustrated in Figures 5a and S57. To mimic seed preparation by sonication, a short cylinder was directly cut from the prepared cylinders to serve as the seed for epitaxial growth to fabricate 2D platelets (Figure 5a). The living CDSA process was successfully simulated, revealing that the  $R_7C_4$  block copolymer (PCL<sub>51</sub>-*b*-PDMA<sub>189</sub>) predominantly localizes at the edges of the platelets, while the  $R_7$  homopolymer (PCL<sub>51</sub>) is situated within the interior of the platelets. The simulation results show the block copolymer  $R_7C_4$  (PCL<sub>51</sub>-*b*-PDMA<sub>189</sub>) is primarily distributed along the

edges of the platelets, while the  $R_7$  homopolymer (PCL<sub>51</sub>) is concentrated in the center. This distribution indicates that the crystallization rate of the PCL<sub>51</sub> homopolymer is faster than that of the PCL<sub>51</sub>-*b*-PDMA<sub>189</sub> block copolymer (Figure S58), which is consistent with our experimental observations, supporting the proposed structural arrangement within the platelets. Additionally, the preparation of multilayered platelets was investigated. The sequential addition of unimers successfully promoted growth at the edges of the preformed platelets at each step, resulting in progressively larger 2D platelets (Figure S58). This observation demonstrates that the 2D platelets obtained from each growth phase retain their crystalline surface activity for further living growth.

To investigate the influence of PCL length on crystallization behavior via BD simulation, the seeded growth of 2D platelets was monitored upon the addition of different PCL HP ( $R_m$ ,  $m = 4, 7, \text{ or } 11$ ) and PCL-*b*-PDMA BCP ( $R_7C_4$ ) blends. When the length of the homopolymer was changed, platelets with different aspect ratios were obtained (Figures 5b,5c and S59). The results demonstrate that the crystallization rate of platelets in both the long axis ( $L_a$ ) and short axis ( $L_b$ ) directions is influenced by the length of PCL homopolymer, and using shorter PCL can result in platelets with larger aspect ratios, which aligns with experimental results.

Additionally, the orientation arrangement variation of PCL crystallizable chains before and after seeded growth has been tracked. The local order of individual polymer chains and the overall order of 2D platelets were quantitatively described by the tilt angles  $\theta$  and  $\varphi$  (Figure 5d), respectively (where  $\theta$  represents the angle between PCL folding chains within a single polymer chain, while  $\varphi$  represents the angle between all PCL chains and the axis perpendicular to the central axis of the platelet). The distributions of  $\text{lc}os\ \theta$  and  $\text{lc}os\ \varphi$  have been plotted. For the PCL chain folding in the cylinder and seeds (green region), the distributions of  $\text{lc}os\ \theta$  and  $\text{lc}os\ \varphi$  are both narrow, ranging between 0.9 and 1.0 (Figure 5e), indicating that the PCL chains are arranged in a mutually parallel manner during crystallization folding and are uniformly oriented perpendicular to the growth plane. For the subsequent living CDSA process (blue region), most PCL chains participate in assembly and crystallization by folding in a mutually parallel manner, which is similar to that in the seeds. The PCL chains throughout the entire 2D platelet are almost uniformly oriented perpendicular to the plane of the entire 2D platelet (Figure 5f). The ordered arrangement of PCL chains during crystallization growth has been simulated, indicating that the PCL chains in the 2D platelets grown by crystallization adopt a consistent arrangement with the initial seed micelles to achieve internally ordered and morphologically controllable 2D platelets. Thus, the simulation results not only align with the experimental findings but also enhance our understanding of the CDSA process.

## CONCLUSIONS

This study delves into the precise modulation of the aspect ratio and polymer spatial distribution in 2D platelets through living crystallization-driven self-assembly (CDSA). By systematically varying the core and corona lengths of polymers, we uncovered the intricate interplay between polymer composition, crystallization kinetics, and the resulting nanostructure morphology. Through experimental investigations, we demonstrated the significant impact of polymer chain length on platelet aspect ratio, with shorter polymer chains leading to

higher aspect ratios due to slower crystallization rates preferring growth from a lower surface energy crystalline plane (110). The “jumping aspect ratio” platelets further highlighted the tunability of platelet shape by alternately adding short and long PCL chain homopolymers. Furthermore, the simultaneous influence of homopolymers and block copolymers on platelet morphology was explored, providing insights into the effects of different polymer compositions. Complementing our experimental findings, the Brownian dynamics (BD) method simulated the crystallization behavior during the CDSA process, revealing the ordered arrangement of polymer chains within the platelets and the influence of PCL length on aspect ratio. These simulations confirmed the experimental observations and provided detailed insights into platelet formation. Overall, our study advances the fundamental understanding of aspect ratio control in anisotropic nanostructures and offers valuable insights into designing and fabricating tailored nanomaterials.

## ASSOCIATED CONTENT

### Supporting Information

The Supporting Information is available free of charge at <https://pubs.acs.org/doi/10.1021/acs.macromol.4c02496>.

Materials, characterization, instrumentation, methods, experimental procedures, and additional data (NMR, SEC, TEM, AFM, and CLSM images) (PDF)

## AUTHOR INFORMATION

### Corresponding Authors

Andrew P. Dove – School of Chemistry, University of Birmingham, Birmingham B15 2TT, U.K.; [orcid.org/0000-0001-8208-9309](https://orcid.org/0000-0001-8208-9309); Email: [a.dove@bham.ac.uk](mailto:a.dove@bham.ac.uk)

Rachel K. O'Reilly – School of Chemistry, University of Birmingham, Birmingham B15 2TT, U.K.; [orcid.org/0000-0002-1043-7172](https://orcid.org/0000-0002-1043-7172); Email: [r.oreilly@bham.ac.uk](mailto:r.oreilly@bham.ac.uk)

### Authors

Tianlai Xia – School of Chemistry, University of Birmingham, Birmingham B15 2TT, U.K.; [orcid.org/0000-0002-4391-0296](https://orcid.org/0000-0002-4391-0296)

Laihui Xiao – School of Chemistry, University of Birmingham, Birmingham B15 2TT, U.K.; [orcid.org/0000-0002-3412-0954](https://orcid.org/0000-0002-3412-0954)

Kaiwen Sun – Shanghai Key Laboratory of Advanced Polymeric Materials, Key Laboratory for Ultrafine Materials of Ministry of Education, Frontiers Science Center for Materiobiology and Dynamic Chemistry, School of Materials Science and Engineering, East China University of Science and Technology, Shanghai 200237, China

Julia Y. Rho – School of Chemistry, University of Birmingham, Birmingham B15 2TT, U.K.

Yujie Xie – School of Medicine, Shanghai University, Shanghai 200444, China; [orcid.org/0000-0002-6024-7019](https://orcid.org/0000-0002-6024-7019)

Sam J. Parkinson – School of Chemistry, University of Birmingham, Birmingham B15 2TT, U.K.; [orcid.org/0000-0002-4103-945X](https://orcid.org/0000-0002-4103-945X)

Leire Sangroniz – POLYMAT and Department of Polymers and Advanced Materials: Physics, Chemistry and Technology, Faculty of Chemistry, University of the Basque Country UPV/EHU, 20018 Donostia-San Sebastián, Spain; [orcid.org/0000-0003-0714-3154](https://orcid.org/0000-0003-0714-3154)

**Jian Zhang** – School of Chemistry, University of Birmingham, Birmingham B15 2TT, U.K.; College of Material and Textile Engineering, Jiaying University, Jiaying 314001, China

**Jiaping Lin** – Shanghai Key Laboratory of Advanced Polymeric Materials, Key Laboratory for Ultrafine Materials of Ministry of Education, Frontiers Science Center for Materiobiology and Dynamic Chemistry, School of Materials Science and Engineering, East China University of Science and Technology, Shanghai 200237, China; [orcid.org/0000-0001-9633-4483](https://orcid.org/0000-0001-9633-4483)

**Alejandro J. Müller** – POLYMAT and Department of Polymers and Advanced Materials: Physics, Chemistry and Technology, Faculty of Chemistry, University of the Basque Country UPV/EHU, 20018 Donostia-San Sebastián, Spain; IKERBASQUE, Basque Foundation for Science, Bilbao 48009, Spain; [orcid.org/0000-0001-7009-7715](https://orcid.org/0000-0001-7009-7715)

**Liang Gao** – Shanghai Key Laboratory of Advanced Polymeric Materials, Key Laboratory for Ultrafine Materials of Ministry of Education, Frontiers Science Center for Materiobiology and Dynamic Chemistry, School of Materials Science and Engineering, East China University of Science and Technology, Shanghai 200237, China; [orcid.org/0000-0001-6852-8301](https://orcid.org/0000-0001-6852-8301)

Complete contact information is available at:  
<https://pubs.acs.org/10.1021/acs.macromol.4c02496>

### Author Contributions

○T.X. and L.X. contributed equally to this work. The manuscript was written with contributions from all authors.

### Notes

The authors declare no competing financial interest.

### ACKNOWLEDGMENTS

T.X., J.Y.R., S.J.P., A.P.D., and R.K.O.R. thank the University of Birmingham for financial support. L.X. and J.Z. thank the China Scholarship Council for support. K.S., L.G., and J.L. thank the National Natural Science Foundation of China for financial support (22103025). Y.X. would like to thank the National Natural Science Foundation of China for financial support (22205133). L.S. and A.J.M. would like to acknowledge funding from the project MAT2017-83014-C2-1-P by MCIN/AEI/10.13039/501100011033 and by the Basque Government through grant IT1503-22. We thank Dr. Joao Correia for assistance with fluorescence characterization, and Dr. Joshua Deakin for assistance with XRD characterization.

### REFERENCES

- (1) Hughes, M. D. G.; Cussons, S.; Hanson, B. S.; Cook, K. R.; Feller, T.; Mahmoudi, N.; Baker, D. L.; Ariens, R.; Head, D. A.; Brockwell, D. J.; Dougan, L. Building block aspect ratio controls assembly, architecture, and mechanics of synthetic and natural protein networks. *Nat. Commun.* **2023**, *14* (1), No. 5593.
- (2) Hales, T. C. The Honeycomb Conjecture. *Discrete Comput. Geom.* **2001**, *25* (1), 1–22.
- (3) Demirer, G. S.; Zhang, H.; Matos, J. L.; Goh, N. S.; Cunningham, F. J.; Sung, Y.; Chang, R.; Aditham, A. J.; Chio, L.; Cho, M. J.; Staskawicz, B.; Landry, M. P. High aspect ratio nanomaterials enable delivery of functional genetic material without DNA integration in mature plants. *Nat. Nanotechnol.* **2019**, *14* (5), 456–464.
- (4) Boott, C. E.; Gwyther, J.; Harniman, R. L.; Hayward, D. W.; Manners, I. Scalable and uniform 1D nanoparticles by synchronous polymerization, crystallization and self-assembly. *Nat. Chem.* **2017**, *9* (8), 785–792.

- (5) Sneyd, A. J.; Fukui, T.; Palecek, D.; Prophan, S.; Wagner, I.; Zhang, Y.; Sung, J.; Collins, S. M.; Slater, T. J. A.; Andaji-Garmaroudi, Z.; MacFarlane, L. R.; Garcia-Hernandez, J. D.; Wang, L.; Whittell, G. R.; Hodgkiss, J. M.; Chen, K.; Beljonne, D.; Manners, I.; Friend, R. H.; Rao, A. Efficient energy transport in an organic semiconductor mediated by transient exciton delocalization. *Sci. Adv.* **2021**, *7* (32), No. eabh4232.

- (6) Tian, J.; Zhang, Y.; Du, L.; He, Y.; Jin, X.-H.; Pearce, S.; Eloi, J.-C.; Harniman, R. L.; Alibhai, D.; Ye, R.; Phillips, D. L.; Manners, I. Tailored self-assembled photocatalytic nanofibres for visible-light-driven hydrogen production. *Nat. Chem.* **2020**, *12* (12), 1150–1156.

- (7) Cai, J.; Li, C.; Kong, N.; Lu, Y.; Lin, G.; Wang, X.; Yao, Y.; Manners, I.; Qiu, H. Tailored multifunctional micellar brushes via crystallization-driven growth from a surface. *Science* **2019**, *366* (6469), 1095–1098.

- (8) Tian, J.; Xie, S. H.; Borucu, U.; Lei, S.; Zhang, Y.; Manners, I. High-resolution cryo-electron microscopy structure of block copolymer nanofibres with a crystalline core. *Nat. Mater.* **2023**, *22* (6), 786–792.

- (9) Tong, Z.; Xie, Y.; Arno, M. C.; Zhang, Y.; Manners, I.; O'Reilly, R. K.; Dove, A. P. Uniform segmented platelet micelles with compositionally distinct and selectively degradable cores. *Nat. Chem.* **2023**, *15* (6), 824–831.

- (10) Brisson, E. R. L.; Worthington, M. J. H.; Kerai, S.; Mullner, M. Nanoscale polymer discs, toroids and platelets: a survey of their syntheses and potential applications. *Chem. Soc. Rev.* **2024**, *53* (4), 1984–2021.

- (11) Jin, B.; Li, Q.; Hu, L.; Liu, Q.; Chen, Y.; Luo, Y.; Chi, S.; Li, X. In situ Nucleation-Growth Strategy for Controllable Heterogeneous Supramolecular Polymerization of Liquid Crystalline Block Copolymers and Their Hierarchical Assembly. *Angew. Chem., Int. Ed.* **2023**, *62* (18), No. e202219067.

- (12) Jiang, J.; Nikbin, E.; Hicks, G.; Song, S.; Liu, Y.; Wong, E. C. N.; Manners, I.; Howe, J. Y.; Winnik, M. A. Polyferrocenylsilane Block Copolymer Spherulites in Dilute Solution. *J. Am. Chem. Soc.* **2023**, *145* (2), 1247–1261.

- (13) Deng, R.; Mao, X.; Pearce, S.; Tian, J.; Zhang, Y.; Manners, I. Role of Competitive Crystallization Kinetics in the Formation of 2D Platelets with Distinct Coronal Surface Patterns via Seeded Growth. *J. Am. Chem. Soc.* **2022**, *144* (41), 19051–19059.

- (14) Xie, Y.; Tong, Z.; Xia, T.; Worch, J. C.; Rho, J. Y.; Dove, A. P.; O'Reilly, R. K. 2D Hierarchical Microbarcodes with Expanded Storage Capacity for Optical Multiplex and Information Encryption. *Adv. Mater.* **2024**, *36* (8), No. e2308154.

- (15) Shen, D.; Shi, B.; Zhou, P.; Li, D.; Wang, G. Temperature-Dependent Ring-Opening Polymerization-Induced Self-Assembly Using Crystallizable Polylactones as Core-Forming Blocks. *Macromolecules* **2023**, *56* (13), 4814–4822.

- (16) Li, M.; Guo, J.; Zhang, C.; Che, Y.; Yi, Y.; Liu, B. Uniform Colloidal Polymer Rods by Stabilizer-Assisted Liquid-Crystallization-Driven Self-Assembly. *Angew. Chem.* **2023**, No. e202309914.

- (17) Zhang, Y.; Tian, J.; Shaikh, H.; MacKenzie, H. K.; He, Y.; Zhao, C.; Lei, S.; Ren, Y.; Manners, I. Tailored Energy Funneling in Photocatalytic pi-Conjugated Polymer Nanofibers for High-Performance Hydrogen Production. *J. Am. Chem. Soc.* **2023**, *145* (41), 22539–22547.

- (18) Hurst, P. J.; Rakowski, A. M.; Patterson, J. P. Ring-opening polymerization-induced crystallization-driven self-assembly of poly-L-lactide-block-polyethylene glycol block copolymers (ROPI-CDSA). *Nat. Commun.* **2020**, *11* (1), No. 4690.

- (19) Guo, Y.; Xia, T.; Walter, V.; Xie, Y.; Rho, J.; Xiao, L.; O'Reilly, R.; Wallace, M. Real-time label-free imaging of living crystallization-driven self-assembly. **2024** DOI: [10.26434/chemrxiv-2024-d1gd3](https://doi.org/10.26434/chemrxiv-2024-d1gd3).

- (20) Liu, L. P.; Ferguson, C. T. J.; Zhu, L. Y.; Chen, S. C.; Wang, R. Y.; Wang, S.; Dove, A. P.; O'Reilly, R. K.; Tong, Z. Z. Synthesis of hollow platelet polymer particles by spontaneous precision fragmentation. *Nat. Synth.* **2024**, *3* (7), 903–912.

- (21) Teng, F.; Xiang, B.; Liu, L.; Varlas, S.; Tong, Z. Precise Control of Two-Dimensional Hexagonal Platelets via Scalable, One-Pot

Assembly Pathways Using Block Copolymers with Crystalline Side Chains. *J. Am. Chem. Soc.* **2023**, *145* (51), 28049–28060.

(22) Xie, Y.; Yu, W.; Xia, T.; O'Reilly, R. K.; Dove, A. P. Stereocomplex-Driven Morphological Transition of Coil–Rod–Coil Poly(lactic acid)-Based Cylindrical Nanoparticles. *Macromolecules* **2023**, *56* (19), 7689–7697.

(23) Yang, S.; Kang, S. Y.; Choi, T. L. Semi-conducting 2D rectangles with tunable length via uniaxial living crystallization-driven self-assembly of homopolymer. *Nat. Commun.* **2021**, *12* (1), No. 2602.

(24) Qiu, H.; Gao, Y.; Boott, C. E.; Gould, O. E.; Harniman, R. L.; Miles, M. J.; Webb, S. E.; Winnik, M. A.; Manners, I. Uniform patchy and hollow rectangular platelet micelles from crystallizable polymer blends. *Science* **2016**, *352* (6286), 697–701.

(25) Qi, R.; Zhu, Y.; Han, L.; Wang, M.; He, F. Rectangular Platelet Micelles with Controlled Aspect Ratio by Hierarchical Self-Assembly of Poly(3-hexylthiophene)-*b*-poly(ethylene glycol). *Macromolecules* **2020**, *53* (15), 6555–6565.

(26) Pearce, S.; He, X. M.; Hsiao, M. S.; Harniman, R. L.; MacFarlane, L. R.; Manners, I. Uniform, High-Aspect-Ratio, and Patchy 2D Platelets by Living Crystallization-Driven Self-Assembly of Crystallizable Poly(ferrocenyldimethylsilane)-Based Homopolymers with Hydrophilic Charged Termini. *Macromolecules* **2019**, *52* (16), 6068–6079.

(27) Zhou, T.; Qi, H.; Han, L.; Barbash, D.; Li, C. Y. Towards controlled polymer brushes via a self-assembly-assisted-grafting-to approach. *Nat. Commun.* **2016**, *7*, No. 11119.

(28) Ganda, S.; Stenzel, M. H. Concepts, fabrication methods and applications of living crystallization-driven self-assembly of block copolymers. *Prog. Polym. Sci.* **2020**, *101*, No. 101195.

(29) He, W.-N.; Xu, J.-T. Crystallization assisted self-assembly of semicrystalline block copolymers. *Prog. Polym. Sci.* **2012**, *37* (10), 1350–1400.

(30) Michell, R. M.; Müller, A. J. Confined crystallization of polymeric materials. *Prog. Polym. Sci.* **2016**, *54*–55, 183–213.

(31) Wang, J.; Si, J.; Zhu, J.; Nie, Y.; Lu, Y.; Chen, Y. Effect of block ratios on self-assembly morphologies of poly( $\epsilon$ -caprolactone)-block-poly(*tert*-butyl acrylate) block copolymer. *Polymer* **2023**, *284*, No. 126292.

(32) Yao, Z.-F.; Wang, J.-Y.; Pei, J. Controlling morphology and microstructure of conjugated polymers via solution-state aggregation. *Prog. Polym. Sci.* **2023**, *136*, No. 101626.

(33) Ungar, G.; Putra, E. G. R.; de Silva, D. S. M.; Shcherbina, M. A.; Waddon, A. J. *Interphases and Mesophases in Polymer Crystallization*, 2005.

(34) Sadler, D. M.; Gilmer, G. H. Rate-theory model of polymer crystallization. *Phys. Rev. Lett.* **1986**, *56* (25), 2708–2711.

(35) Kato, S.; Furukawa, S.; Aoki, D.; Goseki, R.; Oikawa, K.; Tsuchiya, K.; Shimada, N.; Maruyama, A.; Numata, K.; Otsuka, H. Crystallization-induced mechanofluorescence for visualization of polymer crystallization. *Nat. Commun.* **2021**, *12* (1), No. 126.

(36) Zhang, S. J.; Wang, Z. Q.; Guo, B. H.; Xu, J. Secondary nucleation in polymer crystallization: A kinetic view. *Polym. Cryst.* **2021**, *4* (3), No. e10173.

(37) Zhang, X.; Chen, G.; Zheng, B.; Wan, Z.; Liu, L.; Zhu, L.; Xie, Y.; Tong, Z. Uniform Two-Dimensional Crystalline Platelets with Tailored Compositions for pH Stimulus-Responsive Drug Release. *Biomacromolecules* **2023**, *24* (2), 1032–1041.

(38) Parkin, H. C.; Street, S. T. G.; Gowen, B.; Da-Silva-Correa, L. H.; Hof, R.; Buckley, H. L.; Manners, I. Mechanism of Action and Design of Potent Antibacterial Block Copolymer Nanoparticles. *J. Am. Chem. Soc.* **2024**, *146* (8), 5128–5141.

(39) Jin, X. H.; Price, M. B.; Finnegan, J. R.; Boott, C. E.; Richter, J. M.; Rao, A.; Menke, S. M.; Friend, R. H.; Whittell, G. R.; Manners, I. Long-range exciton transport in conjugated polymer nanofibers prepared by seeded growth. *Science* **2018**, *360* (6391), 897–900.

(40) Yang, S.; Kang, S. Y.; Choi, T. L. Morphologically Tunable Square and Rectangular Nanosheets of a Simple Conjugated

Homopolymer by Changing Solvents. *J. Am. Chem. Soc.* **2019**, *141* (48), 19138–19143.

(41) Cha, Y.; Jarrett-Wilkins, C.; Rahman, M. A.; Zhu, T.; Sha, Y.; Manners, I.; Tang, C. Crystallization-Driven Self-Assembly of Metallo-Polyelectrolyte Block Copolymers with a Polycaprolactone Core-Forming Segment. *ACS Macro Lett.* **2019**, *8* (7), 835–840.

(42) Kinnear, C.; Moore, T. L.; Rodriguez-Lorenzo, L.; Rothen-Rutishauser, B.; Petri-Fink, A. Form Follows Function: Nanoparticle Shape and Its Implications for Nanomedicine. *Chem. Rev.* **2017**, *117* (17), 11476–11521.

(43) Pearce, A. K.; Wilks, T. R.; Arno, M. C.; O'Reilly, R. K. Synthesis and applications of anisotropic nanoparticles with precisely defined dimensions. *Nat. Rev. Chem.* **2021**, *5* (1), 21–45.

(44) Shi, Y.; Lyu, Z.; Zhao, M.; Chen, R.; Nguyen, Q. N.; Xia, Y. Noble-Metal Nanocrystals with Controlled Shapes for Catalytic and Electrocatalytic Applications. *Chem. Rev.* **2021**, *121* (2), 649–735.

(45) Xia, T.; Tong, Z.; Xie, Y.; Arno, M. C.; Lei, S.; Xiao, L.; Rho, J. Y.; Ferguson, C. T. J.; Manners, I.; Dove, A. P.; O'Reilly, R. K. Tuning the Functionality of Self-Assembled 2D Platelets in the Third Dimension. *J. Am. Chem. Soc.* **2023**, *145* (46), 25274–25282.

(46) Xiao, L.; Parkinson, S. J.; Xia, T.; Edge, P.; O'Reilly, R. K. Enhancing the Scalability of Crystallization-Driven Self-Assembly Using Flow Reactors. *ACS Macro Lett.* **2023**, *12* (12), 1636–1641.

(47) Fernández-Tena, A.; Pérez-Camargo, R. A.; Coulembier, O.; Sangroniz, L.; Aranburu, N.; Guerrica-Echevarria, G.; Liu, G.; Wang, D.; Cavallo, D.; Müller, A. J. Effect of Molecular Weight on the Crystallization and Melt Memory of Poly( $\epsilon$ -caprolactone) (PCL). *Macromolecules* **2023**, *56* (12), 4602–4620.

(48) Hu, W.; Safari, M.; Zhou, Y.; Pérez-Camargo, R. A.; Liu, G.; Müller, A. J.; Wang, D. Comonomer Inclusion in Single Crystals of Isodimorphic Random Copolymers of Butylene Succinate and  $\epsilon$ -Caprolactone. *Macromolecules* **2023**, *56* (13), 5058–5067.

(49) Sangroniz, L.; Cavallo, D.; Müller, A. J. Self-Nucleation Effects on Polymer Crystallization. *Macromolecules* **2020**, *53* (12), 4581–4604.

(50) Mansfield, M. Solution of the growth equations of a sector of a polymer crystal including consideration of the changing size of the crystal. *Polymer* **1988**, *29* (10), 1755–1760.

(51) Frank, F. C. Nucleation-controlled growth on a one-dimensional growth of finite length. *J. Cryst. Growth* **1974**, *22* (3), 233–236.

(52) Gedde, U. W.; Hedenqvist, M. S. *Fundamental Polymer Science*; Springer: Cham, 2019.

(53) Hu, H.; Dorset, D. L. Crystal structure of poly(*i* $\epsilon$ -caprolactone). *Macromolecules* **1990**, *23* (21), 4604–4607.

(54) Hoffman, J. D.; Miller, R. L. Kinetic of crystallization from the melt and chain folding in polyethylene fractions revisited: theory and experiment. *Polymer* **1997**, *38* (13), 3151–3212.

(55) Organ, S. J.; Keller, A. Solution crystallization of polyethylene at high temperatures. *J. Mater. Sci.* **1985**, *20* (5), 1571–1585.

(56) Vyazovkin, S. Activation Energies and Temperature Dependencies of the Rates of Crystallization and Melting of Polymers. *Polymers* **2020**, *12* (5), 1070.

(57) Jin, X.; Zhang, C.; Lin, J.; Cai, C.; Chen, J.; Gao, L. Fusion Growth of Two-Dimensional Disklike Micelles via Liquid-Crystallization-Driven Self-Assembly. *Macromolecules* **2022**, *55* (10), 3831–3839.

(58) Zhang, C.; Lin, J.; Wang, L.; Gao, L. 2D Liquid-Crystallization-Driven Self-Assembly of Rod-Coil Block Copolymers: Living Growth and Self-Similarity. *J. Phys. Chem. Lett.* **2022**, *13* (26), 6215–6222.

(59) Yao, Y.; Gao, L.; Cai, C.; Lin, J.; Lin, S. Supramolecular Polymerization of Polymeric Nanorods Mediated by Block Copolymers. *Angew. Chem., Int. Ed.* **2023**, *62* (9), No. e202216872.